Direct numerical simulation of a fully developed turbulent square duct flow up to $Re_\tau = 1200$

Hao Zhang[a,b], F. Xavier Trias[a], Andrey Gorobets[a,c], Yuanqiang Tan[d], Assensi Oliva[a,*]

[a] *Heat and Mass Transfer Technological Center, Technical University of Catalonia, Terrassa, Barcelona 08222, Spain*
[b] *Key Laboratory of Energy Thermal Conversion and Control of Ministry of Education, School of Energy and Environment, Southeast University, Nanjing, Jiangsu 210096, China*
[c] *Keldysh Institute of Applied Mathematics of RAS, 4A, Miusskaya Sq., Moscow, 125047, Russia*
[d] *School of Mechanical Engineering, Xiangtan University, Hunan 411105, China*

Abstract

Various fundamental studies based on a turbulent duct flow have gained popularity including heat transfer, magnetohydrodynamics as well as particle-laden transportation. An accurate prediction on the turbulent flow field is critical for these researches. However, the database of the mean flow and turbulence statistics is fairly insufficient due to the enormous cost of numerical simulation at high Reynolds number. This paper aims at providing available information by conducting several Direct Numerical Simulations (DNS) on turbulent duct flows at $Re_\tau = 300$, 600, 900 and 1200. A quantitative comparison between current and previous DNS results was performed where a good agreement was achieved at $Re_\tau = 300$. However, further comparisons of the present results with the previous DNS results at $Re_\tau = 600$ obtained with much coarser meshes revealed some discrepancies which can be explained by the insufficient mesh resolution. At last, the mean flow and turbulent statistics at higher Re_τ was presented and the effect of Re_τ on the mean flow and flow dynamics was discussed.

Keywords: Direct Numerical Simulation, Turbulent Flow, Square Duct

[*] Corresponding author
Email addresses: hao@cttc.upc.edu (Hao Zhang), cttc@cttc.upc.edu (Assensi Oliva)

1. Introduction

Turbulent flow transportation through a straight square duct emerges a unique feature due to the existence of the so-called secondary flow of Prandtl's second kind which consists of four pairs of counter-rotating vortexes normal to the stream-wise direction. Statistically, these eight vortexes distribute symmetrically about the bisectors of the walls and the diagonals of the square cross-sections. The first experimental work observing this phenomenon was conducted by Nikuradse [1]. However, the instantaneous flow fields could show fairly stronger vortexes and more complex patterns due to the chaotic changes in the turbulent structure. The problems involved are often too complex to be analyzed analytically or observed by physical experiments. Therefore, they have to be investigated by means of numerical simulations.

Among the most commonly used numerical methodologies are the Direct Numerical Simulation (DNS), the Large Eddy Simulation (LES) and the solution of the Reynolds-Averaged Navier-Stokes equations (RANS). A brief summary of these works relevant to turbulent duct flows are listed in Table 1 classified according to the Re_τ of interest. As shown, various fundamental studies based on a turbulent duct flow have gained popularity including heat transfer, magnetohydrodynamics as well as the particle-laden turbulent flows, etc. An accurate prediction on the turbulent flow field is critical for these researches. DNS is an essential tool to give insights into the physics of turbulence and to provide indispensable data for future progresses on turbulence modeling. However, the DNS database of the turbulent duct flows is fairly insufficient due to the enormous cost at high Re_τ. The first available DNS work was conducted by Gavrilakis [2] at $Re_\tau = 300$ in which a detailed description of the mean flow in the transverse plane and turbulent statistics along the wall bisectors were presented. Thereafter, this database has been adopted as a benchmark purpose either to tune one's turbulent model or verify the code. Joung et al. [3] and Pinelli et al. [4] performed a series of DNS at $Re_\tau = 300$ to pursuit the basic physical mechanisms responsible for the Prandtl's secondary motion of the second kind. Xu [5]

Re_τ	DNS	LES	RANS
≈ 300	Gavrilakis [2], Joung et al. [3], Pinelli et al. [4], Xu [5].	Madabhushi et al. [6], Xu [7].	
	Heat transfer by Piller and Nobile [8], Ma et al. [9].	Heat transfer by Pallares et al. [10], Vázquez et al. [11].	
	Rotating duct by Yang et al. [12].	Rotating duct by Pallares et al. [13].	
	With particles by Sharma et al. [14], Zhang et al. [15, 16, 17].	With particles by Winkler and Rani [18, 19].	
≈ 600	Huser and Biringen [20, 21], Zhu et al. [22].	Lo et al. [23], Hsu et al. [24, 25], Kim and You [26].	
≥ 900			Raiesi et al. [27].
		Heat transfer by Zhu et al. [28].	Heat transfer by Rokni et al. [29].
		With particles by Fairweather and Yao [30].	With particles by Adams et al. [31].

Table 1: Numerical simulation work relevant to turbulent duct flows.

performed DNS at $Re_\tau = 200$ to investigate the fully developed turbulence in a straight square annular duct with the turbulence-driven secondary-flow generation mechanisms investigated by analyzing the anisotropy of the Reynolds stresses. Huser and Biringen [20] expanded the DNS database by simulating turbulent square duct flow at $Re_\tau = 600$ in which the corner influence on turbulent statistics and on the origin of the secondary flows were explained. Then,

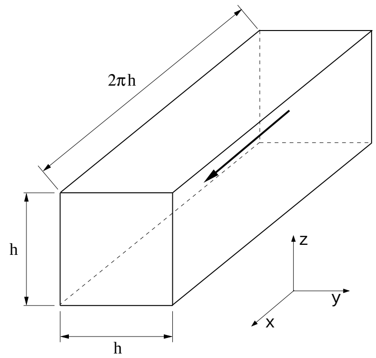

Figure 1: Schema of the square duct.

Huser et al. [21] assessed all the terms in the Reynolds stress transport equation. Zhu et al. [22] examined the turbulent statistics along the wall bisectors at $Re_\tau = 600$. The DNS studies above $Re_\tau = 600$ are quite rare due to the requirement of costly computational resources. For the problems at high Re_τ, an alternative option is to enlarge the range of length scales of the solution by filtering turbulent motions in small scales. LES was particularly popular when special attention was not paid on the slight turbulent flow movement but velocity-coupled heat conduction [28] or behaviors of the floated grain materials [30, 17] where the macro relative velocities between the solid and fluid phases played a key role. Simulations at even higher Re_τ can be achieved using RANS as a cheaper approach whereas inaccuracies of RANS have been reported [31].

As shown in Table 1, a blank exists in the lower left corner. The main object of this study is to partially fill this gap by conducting DNS on a fully developed turbulent duct flow up to $Re_\tau = 1200$. The DNS results in this paper are publicly available in http://www.cttc.upc.edu/downloads/DuctFlow/.

The remainder of this paper is arranged as follows: In Section 2, the governing equations and the numerical procedures are presented. Verification is carried out in Section 3. Numerical simulations are conducted in Section 4 with detailed discussions on the mean flow and turbulence statistics at different Re_τ. Finally, some conclusions are made in Section 5.

2. Governing equations and numerical methods

The incompressible Navier-Stokes (NS) equations in primitive variables are considered

$$\frac{\partial \mathbf{u}}{\partial t} + (\mathbf{u} \cdot \nabla)\, \mathbf{u} = \nu \nabla^2 \mathbf{u} - \nabla p; \qquad \nabla \cdot \mathbf{u} = 0, \tag{1}$$

where $\mathbf{u} = (u, v, w)$ is the velocity field, p represents the kinematic pressure and ν is the kinematic viscosity. A schema of the problem under consideration is displayed in Figure 1. The dimensions of the computational domain are $L_x \times h \times h$ in the stream-wise and wall-normal directions. The Reynolds number based on the friction velocity, u_τ, and the hydraulic diameter, h, is given by $Re_\tau = u_\tau h/\nu$. Periodic boundary conditions are applied in the stream-wise direction. The flow is driven by means of a constant pressure gradient in the stream-wise direction, $dP/dx = 4hu_\tau^2$. Finally, no-slip boundary conditions are imposed at the walls. Therefore, the configuration depends only on the Re_τ and the length aspect ratio, L_x/h. A detailed discussion about the determination of the domain size and grid spacing is given in the next section.

The incompressible Navier-Stokes (NS) equations (1) are discretized on a staggered Cartesian grid using a fourth-order symmetry-preserving discretization [32]. Shortly, the temporal evolution of the spatially discrete staggered velocity vector, $\mathbf{u}_h$, is governed by the following operator-based finite-volume discretization of Eqs.(1)

$$\mathbf{\Omega} \frac{d\mathbf{u}_h}{dt} + \mathbf{C}(\mathbf{u}_h)\, \mathbf{u}_h + \mathbf{D}\mathbf{u}_h - \mathbf{M}^t \mathbf{p}_h = \mathbf{0}_h, \tag{2}$$

where the discrete incompressibility constraint is given by $\mathbf{M}\mathbf{u}_h = \mathbf{0}_h$ and the subscript h refers to discrete vectors. The diffusive matrix, $\mathbf{D}$, is symmetric and positive semi-definite; it represents the integral of the diffusive flux, $-\nu \nabla \mathbf{u} \cdot \boldsymbol{n}$, through the faces. The diagonal matrix, $\mathbf{\Omega}$, describes the sizes of the control volumes and the approximate, convective flux is discretized as in [32]. The resulting convective matrix, $\mathbf{C}(\mathbf{u}_h)$, is skew-symmetric, *i.e.* $\mathbf{C}(\mathbf{u}_h) = -\mathbf{C}^t(\mathbf{u}_h)$. Then, for the temporal discretization, a second-order explicit one-leg scheme is

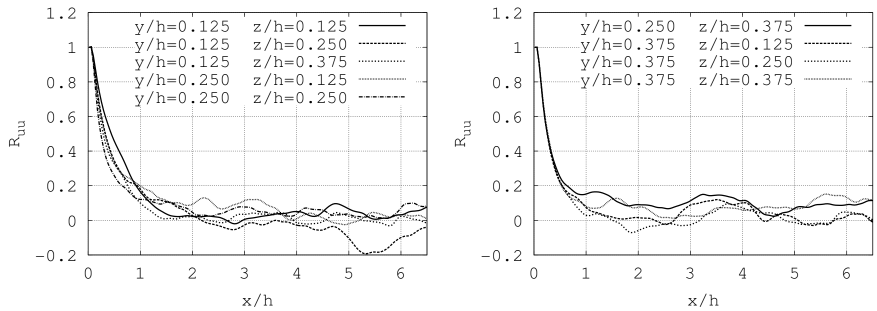

(a) (b)

Figure 2: Two-point correlations of the stream-wise velocity, u, at nine monitoring locations. This case corresponds to a simulation with $L_x/h = 4\pi$, *i.e.* double length that the simulation parameters shown in Table 2.

used for both the convective and the diffusive terms [33]. Finally, the pressure-velocity coupling is solved by means of a classical fractional step projection method [34]: a predictor velocity, $\mathbf{u}_h^p$, is explicitly evaluated without considering the contribution of the pressure gradient. Then, by imposing the incompressibility constraint, $\mathbf{M}\mathbf{u}_h^{n+1} = \mathbf{0}_h$, it leads to a Poisson equation for $\mathbf{p}_h^{n+1}$ to be solved once each time-step,

$$\mathbf{L}\mathbf{p}_h^{n+1} = \mathbf{M}\mathbf{u}_h^p \qquad \text{with} \qquad \mathbf{L} = -\mathbf{M}\mathbf{\Omega}^{-1}\mathbf{M}^t, \tag{3}$$

where the discrete Laplacian operator, $\mathbf{L}$, is represented by a symmetric negative semi-definite matrix. For details about the numerical algorithms and the parallel Poisson solver the reader is referred to [35]. The code was verified using the method of manufactured solutions, and tested for several benchmark reference results. Moreover, since a symmetry-preserving discretization is being used, the exact fulfilment of the global kinetic energy balance was used as an additional verification. For more details about the code verification the reader is referred to our previous work [36]. In addition, rigorous comparison with accurate previous numerical studies [2] of the flow in a straight square duct have been used to verify the code for this configuration. The verification process of the DNS simulations carried out in this work is addressed in the next section.

Re_τ	L_x/h	$N_x \times N_y \times N_z$	L_x^+	L_y^+	Δx^+	Δy^+_{min}	γ	$CPUs$
300	2π	$160 \times 128 \times 128$	1885	300	11.78	0.224	1.85	32
600	2π	$320 \times 256 \times 256$	3770	600	11.78	0.216	1.85	64
900	2π	$480 \times 384 \times 384$	4050	900	11.78	0.215	1.85	196
1200	2π	$640 \times 512 \times 512$	7540	1200	11.78	0.214	1.85	392

Table 2: Physical and numerical simulation parameters.

3. Verification of the simulation

Since no subgrid-scale model is used, the grid resolution and the time step must be fine enough to capture well all the relevant turbulent scales. Moreover, the domain in the periodic direction, L_x, must be long enough, keeping an adequate mesh resolution, Δx, to ensure that numerical solution is not affected. Finally, the starting time for averaging and the time integration period must also be long enough to evaluate the flow statistics properly.

As mentioned above, the results by Gavrilakis [2] have been used to verify the code for this configuration at $Re_\tau = 300$. In a preliminary simulation, we have used a $320 \times 128 \times 128$ Cartesian staggered grid to cover the computational domain with length aspect ratio $L_x/h = 4\pi$, *i.e.* double length (also double number of grid points in the stream-wise direction, N_x) that the simulation parameters shown in Table 2 for $Re_\tau = 300$. This length must be long enough to ensure that turbulent fluctuations are uncorrelated at a separation of one half-period, $L_x/2$. This issue has been discussed in [2], however, a long length ($L_x/h = 10\pi$) was employed by the author for safety. Based on the research of Uhlmann *et al.* [37], the minimum value for the stream-wise length is around 190 wall-units and roughly independently of the Reynolds number. In this study, stream-wise two-point correlations have been carried out to check the domain size in the x-direction. Figure 2 displays results for the stream-wise velocity component, R_{uu}, at nine different (y, z)-locations. For all cases, the correlation values fall to zero for separations lower than one half-period. Similar results are obtained for other (y, z)-locations and variables. Actually, results show that a

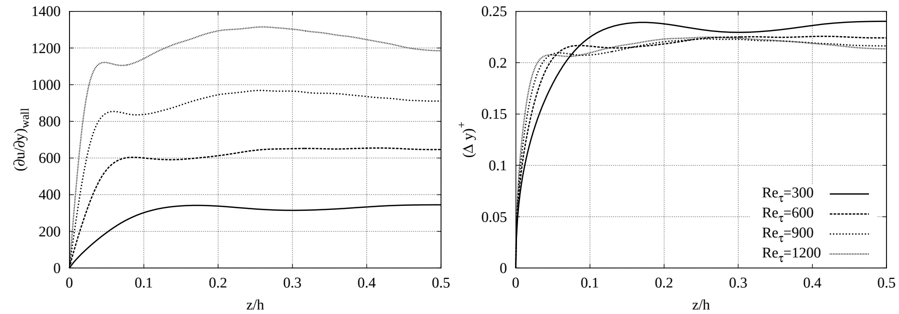

Figure 3: Time-averaged wall-shear stress (left) and location of the first grid point in wall-units (right).

shorter stream-wise length suffices. Hence, in the view of lower cost and better grid resolution in that direction, $L_x/h = 2\pi$ has been used (see Table 2).

Once the physical parameters are controlled, the grid resolution and the time step need to be determined. Grid spacing in the period x-direction is uniform whereas the wall-normal points are distributed using a hyperbolic-tangent function. Namely,

$$y_j = \frac{L_y}{2}\left(1 + \frac{tanh\left\{\gamma\left(2\left(j-1\right)/N_y - 1\right)\right\}}{tanh\gamma}\right), \qquad j = 1, \ldots, N_y + 1. \qquad (4)$$

The grid points in the z-direction are distributed in the same way. Then, the concentration factor, γ, have been chosen equal to the value proposed by Gavrilakis [2]. This and other relevant simulation parameters can be found in Table 2. All the simulations were carried out on the IBM MareNostrum supercomputer which contains 2880 nodes with $2x$ Intel Xeon $E5 - 26708 - core2.6GHz$, 32 GB $DDR3 - 1600$ DIMMS $(2GB/core)$ and Infiniband FDR10. The longest simulation at $Re_\tau = 1200$ took around $800,000$ CPU hours.

The region most sensitive to the grid resolution is near the wall. Figure 3 displays the location of the first grid point in wall-units. Note that in this case the friction velocity, u_τ, is computed with the local wall-shear stress. This value falls down to values smaller than unity for the four Re_τ studied here, indicating that the grid is fine enough. In turbulent regions, the smallest resolved length scale is required to be $\mathcal{O}(\eta)$ where $\eta = (\nu^3/\left\langle\epsilon\right\rangle)^{1/4}$ is the Kolmogorov length

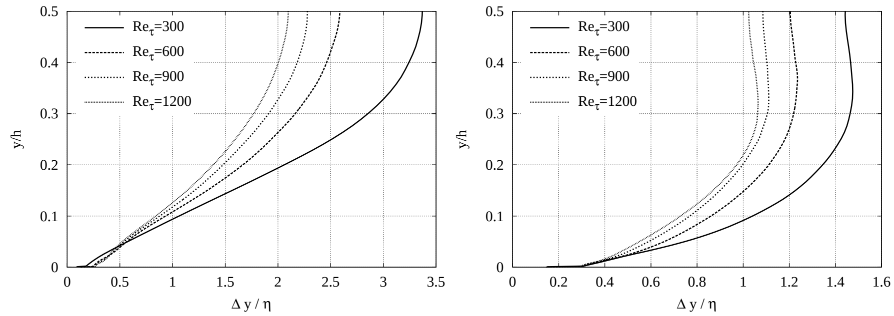

Figure 4: Ratio between the wall-normal grid spacing and the Kolmogorov length scale, η, at $z/h = 0.05$ (left) and $z/h = 0.5$ (right).

scale and $\langle \epsilon \rangle$ is the time-averaged local dissipation of turbulent kinetic energy. Figure 4 displays the ratio between the wall-normal grid spacings, Δy, and η at two different locations. As expected, higher values are observed at $z/h = 0.05$ where values of $\langle \epsilon \rangle$ are higher than in the centerline. The highest values measured are similar to the resolution requirements suggested in [38, 39] to obtain accurate first- and second-order statistics. They follow from the criterion that most of the dissipation is being captured. Therefore, grid spacings equal or smaller than η are considered too stringent because the Kolmogorov length scale is at the far end of the dissipative range. In this regard, a very recent work [40] has shown that most of the dissipation in a turbulent channel flow occurs at scales greater than 30η. In any case, the highest values for the ratio $\Delta y/\eta$ are obtained at $Re_\tau = 300$ for which at excellent agreement has been obtained with the results by Gavrilakis [2]; therefore, meshes at higher Re_τ are also fine enough to resolve all relevant spatial turbulent scales. Regarding the time-step, Δt, it follows from the CFL-like stability criterion proposed in [33]; therefore, it is sufficiently lower than the smallest relevant temporal scale. Starting from an initial velocity field interpolated from a coarser mesh, simulation have been carried out until a statistically steady state is reached. Then, flow statistics have been computed over a period of approximately 20 turnovers (1 turnover $\equiv 0.5h/u_\tau$). In this regard, the time correlation, $R(\tau) = \langle u'(t)u'(t+\tau) \rangle / u_{rms}$, of the stream-wise velocity at $(y^+ = 10, z/h = 0.50)$ and $(y^+ = 10, z/h = 0.60)$

for $Re_\tau = 900$ is displayed in Figure 5. These locations correspond to high-correlation regions, and their integral time scales (expressed in viscous units, τ^+) are ≈ 28.5 and ≈ 17, respectively. Similar values were obtained in the near-wall region of a turbulent channel flow [41]. In this case, one turnover corresponds to $\tau^+ = 450$; therefore, the above-mentioned averaging period corresponds to, at least, ≈ 315 integral time scales.

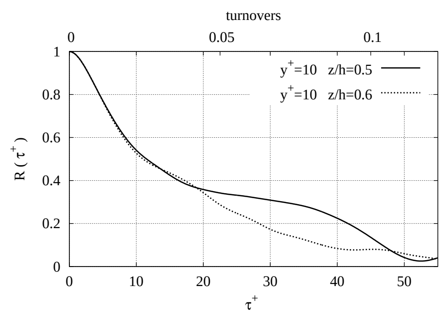

Figure 5: Time correlation of the stream-wise velocity, u, at two locations at $y^+ = 10$ for $Re_\tau = 900$.

4. Results and discussions

In this section, we directly present the numerical results for all Re_τ. Meanwhile, the reliabilities are proved through quantitative comparisons with Gavrilakis [2] at $Re_\tau = 300$ and Huser and Biringen [20] at $Re_\tau = 600$. Averages over the five statistically invariant transformations (time, x-direction, two central planes and diagonal symmetries) are carried out for all the fields. Hence, apart from averaging on time and along the stream-wise direction, this implies an averaging over the 8 quadrant bisectors as well. The standard notation $\langle\cdot\rangle$ is used to denote this averaging procedure. Hence, hereafter we consider that average results depend on y and z but not on x, i.e. $< \phi(y,z) >$.

4.1. The mean velocity field

The mean secondary velocity vectors and stream-wise flow contours in the left lower quadrant are shown in Figure 6 where the mean stream-wise flows are

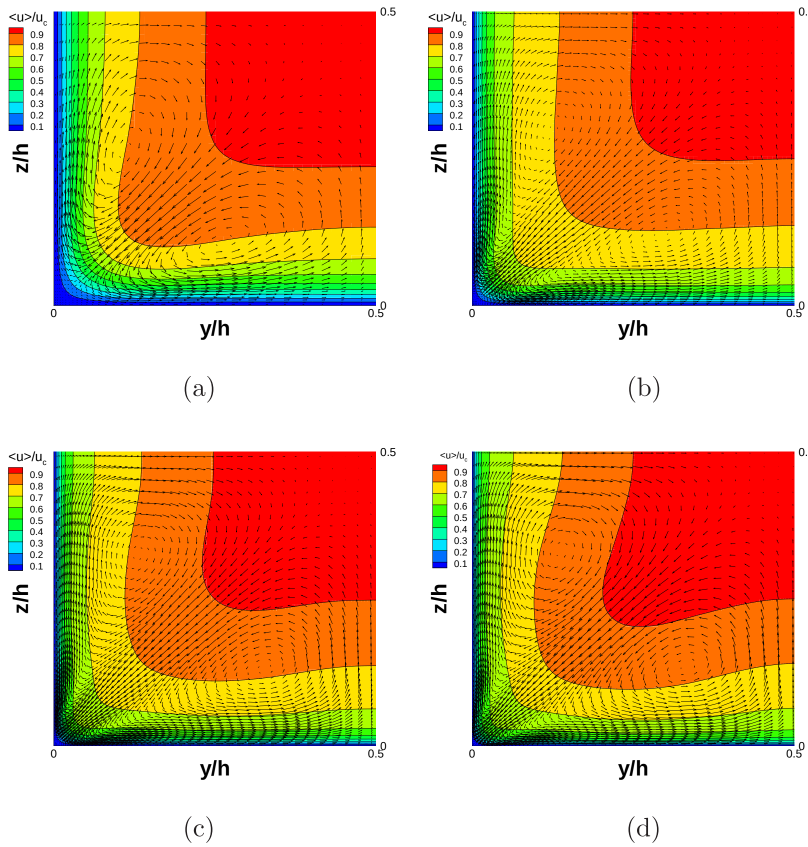

Figure 6: Mean secondary velocity vectors with mean stream-wise flow contours at: (a) $Re_\tau = 300$, (b) $Re_\tau = 600$, (c) $Re_\tau = 900$, (d) $Re_\tau = 1200$.

normalized by the average central velocity, $u_c =< u(h/2, h/2) >$. As expected, there exists a pair of counter-rotating vortexes in each quadrant and it can be seen that the patterns of the secondary vortexes are obviously influenced by Re_τ. The vortex center of the secondary flow moves from the corner to the wall bisector as Re_τ increases. The locations of the lower vortex center $(y/h, z/h)$ are $(0.26, 0.11)$ at $Re_\tau = 300$, $(0.31, 0.13)$ at $Re_\tau = 600$, $(0.33, 0.14)$ at $Re_\tau = 900$ and $(0.33, 0.13)$ at $Re_\tau = 1200$. This finding is in line with the trend reported in [2] and [20]. The effect of Re_τ on the distribution of the mean stream-wise velocity is also obvious. The secondary flows are capable of transferring energy

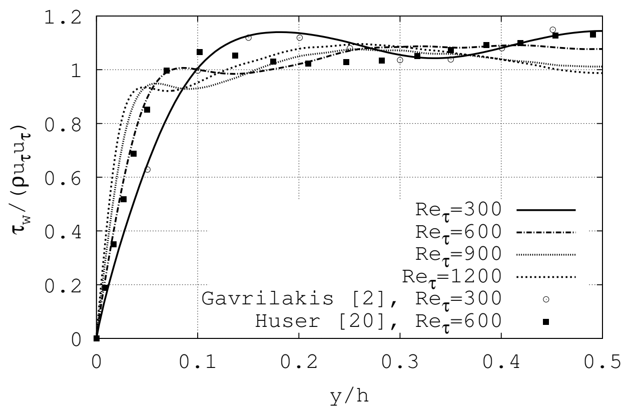

Figure 7: Averaged wall stress variation with data from Gavrilakis [2] and Huser and Biringen [20].

from the center to the corners and thus pushing the high velocity zone toward the corner. As shown, the degree of the influence increases with Re_τ. However, it is worthwhile mentioning that the marginal Reynolds number to show this phenomenon is around $Re_\tau = 160$ below which the flow exhibits totally different secondary flow structures alternating with time [37].

The discrepancy of the secondary vortexes leads to the difference on the distribution of the averaged wall shear stress. They are displayed in Figure 7 together with the results from Gavrilakis ($Re_\tau = 300$) [2] and Huser and Biringen ($Re_\tau = 600$) [20] for comparative purposes. It is shown that the current line at $Re_\tau = 300$ agrees very well with that reported by Gavrilakis [2]. As for $Re_\tau = 600$, consistency between the current result and Huser and Biringen [20] can be only observed near the corner. The two profiles crisscross at the region far from the corner. The discrepancy can be due to the different numerical scheme and grid resolution since the DNS results are quite sensitive to these factors. A stream-wise length of $L_x/h = 2\pi$ has been adopted in both [20] and here whereas the former study employed a much coarser grid resolution ($96 \times 100 \times 100$) than in this study ($320 \times 256 \times 256$). A fine-enough mesh is critical in DNS because the coarse one may also gives rise to an inaccurate prediction on the bulk velocity, u_b, or other flow quantities as shown in Table 3. Based on the current results, two wall stress peaks can be observed at all Re_τ. One is near the corner and the other is near the wall bisector. In the corner region, the gradient of the averaged wall shear stress becomes sharper with the increase of Re_τ. As expected, the location of the first peak approaches to the corner and the magnitude decreases as Re_τ increases. It is interesting to find out that the profile at $Re_\tau = 300$ shows a clearly different trend with higher ones. This low-Reynolds-number effect has been fully discussed in [2] from several aspects. The second peak at low Re_τ is closer to the middle point of duct bottom than high Re_τ. The magnitude of τ_w at the wall bisector drops with the increase of Re_τ.

Re_τ	Reference	u_c/u_b	F_f	u_τ/u_b
300	Present (DNS)	1.33	0.037	0.068
	Gavrilakis (DNS) [2]	1.33	0.037	0.068
	Sharma (DNS) [14]	1.32	0.035	0.066
600	Present (DNS)	1.30	0.031	0.062
	Hartnett (Experiment) [42]	–	0.030	0.061
	Huser (DNS) [20]	–	0.027	0.058
900	Present (DNS)	1.27	0.028	0.059
1200	Present (DNS)	1.26	0.025	0.056

Table 3: Comparison of flow quantities computed in present DNS and others.

Further comparison of flow quantities are presented in Table 3 where the friction factor is defined by the averaged friction and bulk velocities: $F_f = 8u_\tau^2/u_b^2$. It is seen that all the current results obey the trend of the correlation which was proposed based on the experiments of Jones [43]

$$1/F_f^{1/2} = 2log(Re_j F_f^{1/2}) - 0.8 \tag{5}$$

where $Re_j = 1.125Re_b$ stands for the modified Reynolds number for square duct. As for the numerical results, the current result at $Re_\tau = 300$ shows a perfect agreement with Gavrilakis [2] but a little higher than Sharma and Phares [14].

The $Re_\tau = 600$ results are also closer to the experimental observations [42] than Huser and Biringen [20]. All the flow quantities shown in Table 3 tend to decrease as a consequence of the reduction of the boundary layer thickness with Re_τ.

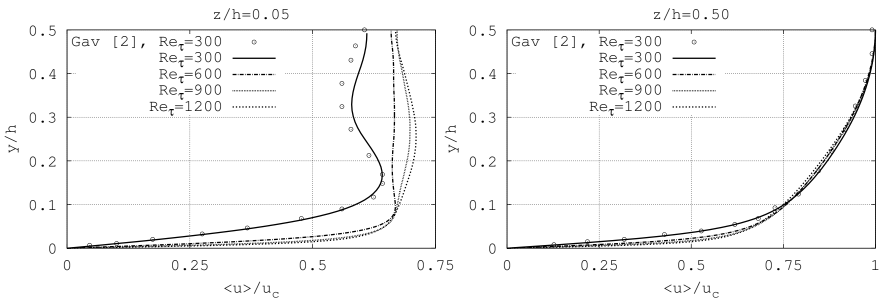

(a) (b)

Figure 8: Profiles of the mean stream-wise velocity near the (a) bottom and (b) wall bisector.

For the sake of clarifying the influence of Re_τ on the mean velocities, Figure 8 and 9 display the distribution of the mean stream-wise and lateral velocities normalized by the averaged central velocity, u_c, respectively. Again, all the current profiles at $Re_\tau = 300$ agree well with those reported by Gavrilakis [2]. The discrepancies close to the wall bisector are due to the different length adopted in the stream-wise direction [2, 14] whereas do not give rise to further differences on the prediction of the averaged qualities. Similar to the averaged wall shear stress distribution, near-wall ($z/h = 0.05$) results at $Re_\tau = 300$ display a significantly different behavior due to the low-Reynolds-number effect. Namely, near the corner ($y/h \leq 0.1, z/h = 0.05$), the gradient of the mean stream-wise velocity is significantly lower than the rest of Re_τ. Far from the corner ($y/h > 0.1, z/h = 0.05$), results are also quite different: a second peak at $y/h = 0.5$ is observed at $Re_\tau = 300$ whereas for the rest of Re_τ the profiles are almost flat. This is because the center of the vortexes moves from the corner to the wall bisector as Re_τ increases. The change on the secondary flow patterns makes further influence of the stream-wise velocities close to the duct bottom. The height of the peak or valley may also increase with Re_τ due to the fact that

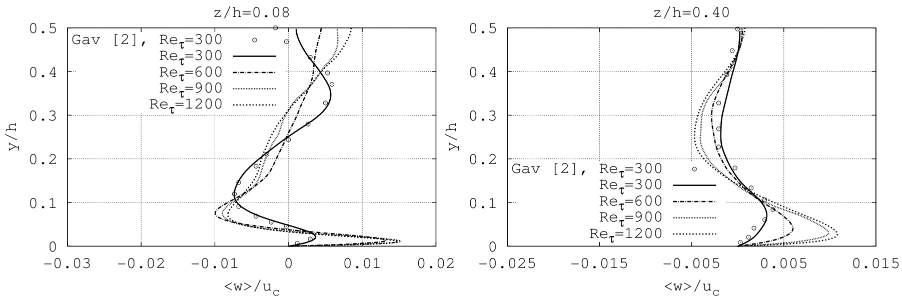

(a) (b)

Figure 9: Profiles of the mean lateral velocity near the (a) bottom and (b) wall bisector.

the secondary vortexes are stronger as Re_τ increases. Figure 8(b) displays the distribution of the stream-wise velocity along the wall bisector. Apart from the obvious differences near the sidewall, results do not seem to be influenced by Re_τ very much because the secondary flow here is relatively weak.

Figure 9 displays the averaged parallel-to-wall velocity normalized by the central velocity at two different locations. This is a good measure of the strength of the secondary flow. As seen in Figure 9 (a), the positive vertical velocity exits close to the duct corner ($y/h \leq 0.05, z/h = 0.08$) which belongs to the upper clockwise-rotating secondary vortex. The upward strength increases with Re_τ. However, the vertical secondary strength seems to be independent of Re_τ at the region far from the sidewall ($y/h > 0.05, z/h = 0.08$). The profiles vary also because the center of the vortex moves from the corner to the wall bisector as discussed above. In Figure 9 (b), $< w > /u_c$ at $z/h = 0.4$ is picked since the vertical secondary strength along the wall bisector is extremely weak. The discrepancy here due to the difference of Re_τ has been expected and obvious. The strength of the secondary flow is found to increase with Re_τ. The trend can be also observed from the secondary flow vectors in Figure 6.

4.2. Turbulent statistics

Unlike the mean values, the instantaneous fields of a turbulent flow are much more complex. For instance, the instantaneous distribution of the vorticity mag-

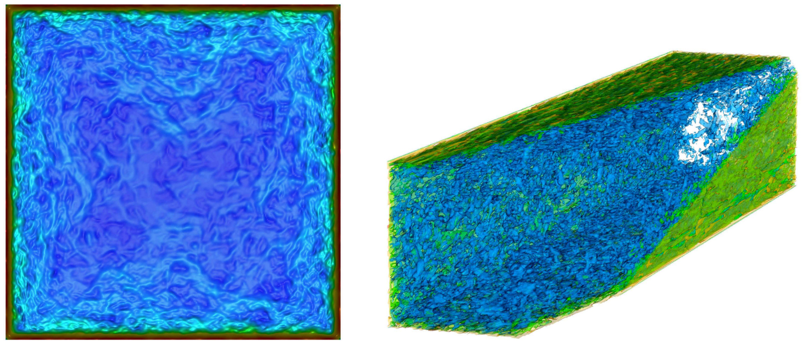

(a) (b)

Figure 10: (a) 2D slice and (b) 3D instantaneous distribution of vorticity magnitude at $Re_\tau = 1200$. Animation is available at http://www.cttc.upc.edu/downloads/DuctFlow/.

nitude at $Re_\tau = 1200$ is displayed in Figure 10. As expected, the patterns exhibit significantly irregular, non-linear and asymmetrical behaviors especially in the 3D snapshot. Such fluctuations around the mean values strongly increase the transport and mixing effects compared with a laminar flow. Therefore, second-order statistics (or turbulent statistics) of the velocity field are fundamental to analyse a turbulent flow.

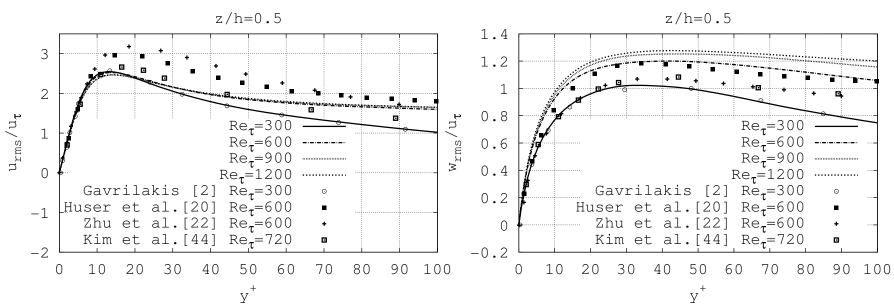

(a) (b)

Figure 11: Distribution of (a) u_{rms}/u_τ, (b) w_{rms}/u_τ along the wall bisector normalized by the local friction velocity.

The turbulence intensities are presented in Figure 11 and 12 where special attention was paid on the behavior near the sidewall ($y^+ \leq 100$). Figure 11 (a)

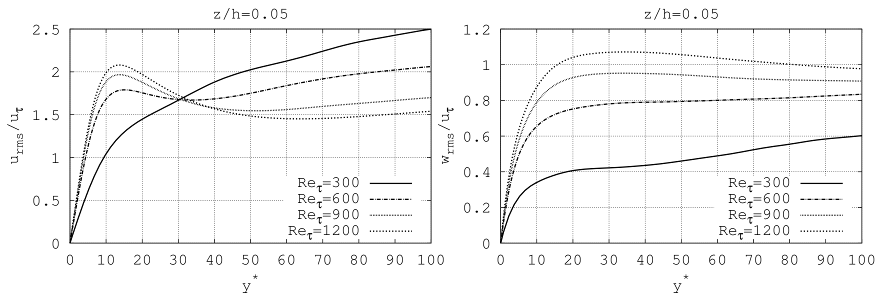

(a) (b)

Figure 12: Comparison of r.m.s. fluctuations near the duct bottom normalized by the local friction velocity: (a) u_{rms}/u_τ, (b) w_{rms}/u_τ.

shows u_{rms}/u_τ distribution along the wall bisector. It can been seen that the current results are in perfect line with previous references in the viscous sublayer ($y^+ < 10$). In the rest of region, the current results are quite comparable with Gavrilakis [2] and Kim et al. [44] whereas significantly lower than the other two DNS works [20, 22] due to their coarse mesh. This finding has been noticed before in [20] and [45] that u_{rms}/u_τ decreases with increasing grid resolution and the maximum value of which has a tendency to over-predicted when using upwind-biased scheme. Further more, our results reveal that u_{rms}/u_τ above $Re_\tau = 600$ is nearly independent of Re_τ at the wall bisector. The lower value at $Re_\tau = 300$ is due to the low-Reynolds-number effect. The magnitude of w_{rms}/u_τ is obviously lower than u_{rms}/u_τ but increases with Re_τ as shown in Figure 11 (b). The current results of w_{rms}/u_τ at the wall bisector are found in line with Gavrilakis [2] and Huser and Biringen [20] at $Re_\tau = 300$ and 600, respectively. But the DNS results of Zhu et al. [22] at $Re_\tau = 600$ are lower than others.

The turbulence intensities near the duct corner at different Re_τ are shown in Figure 12. The magnitude of u_{rms}/u_τ here is comparable with that at the wall bisector. Due to the typical feature of the secondary flow of Prandtl's second kind, the distribution trend of u_{rms}/u_τ switches at about $y^+ = 30$ below which u_{rms}/u_τ increases with Re_τ whereas emerges totally reversed distribution when

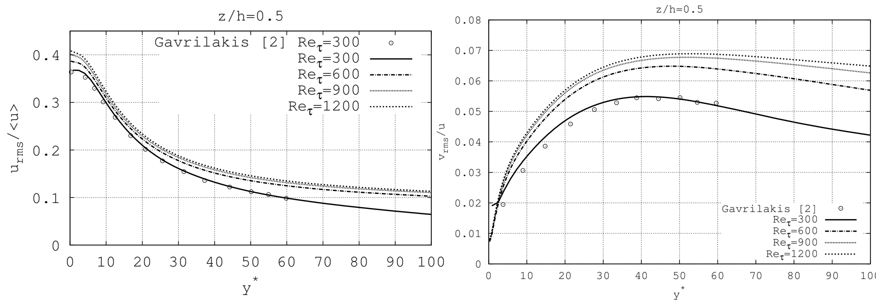

(a) (b)

Figure 13: Variation of the turbulent intensities scaled with the local mean stream-wise.

beyond it. This phenomenon due to the Reynolds-number difference has not been reported before. w_{rms}/u_τ near the duct corner shares similar trends with u_{rms}/u_τ and the magnitude increases with Re_τ as shown in Figure 12 (b).

Finally, as illustrated by Gavrilakis [2], the values for $u_{rms}/ < u >$ and $w_{rms}/ < u >$ close to the sidewall can be regarded as the root-mean-square of the span-wise, ω_z, and stream-wise, ω_x, vorticity scaled with wall variables, respectively. Through a literal survey, suggested values of ω_z are 0.36 by Kim et al. [44] and Gavrilakis [2], 0.38 by Popovich and Hummel [46] and 0.40 by Alfredsson et al. [47]. Figure 13 (a) displays the $u_{rms}/ < u >$ distribution along the wall bisector at different Re_τ. It can be seen that the predicted span-wise components by current DNS range from 0.36 at $Re_\tau = 300$ to 0.41 at $Re_\tau = 1200$ and the magnitude increases with Re_τ. It can be seen in Figure 13 (b) that $w_{rms}/ < u >$ shares the same trend as $u_{rms}/ < u >$ but exhibits a sharp drop at the region very close to the sidewall ($y^+ < 10$) while much flatter in the rest regions.

5. Concluding remarks

Direct numerical simulation of a straight turbulent duct flow has been carried out at $Re_\tau = 300$, 600, 900 and 1200. Cartesian staggered meshes were employed with up to 167.8 millions of nodes. A fully-conservative fourth-order spatial discretization has been used together with a second-order explicit time integration scheme.

A quantitative comparison between current and previous DNS results was performed at $Re_\tau = 300$ where a good agreement was achieved. However, further comparisons of the present results with the previous DNS results at $Re_\tau = 600$ obtained with much coarser meshes revealed some discrepancies which can be explained by the insufficient mesh resolution. The present DNS and the code used for the simulations have been carefully verified in order to provide sufficient mesh resolution and reliablility of the high-order numerical method. At last, the mean flow and turbulent statistics of the turbulent duct flow at higher Re_τ was presented with the effect of Re_τ on the mean and instantaneous velocity field discussed. Our results show that both the mean flow and turbulent statistics can be affected by Re_τ especially close to the duct wall. The pattern and strength of the secondary vortexes vary with Re_τ which leads to further influence on the distribution of the mean stream-wise flow and wall stress. An interesting phenomenon is that $Re_\tau = 600$ stands like a critical Reynolds number below which the fluid exhibits behavior with large discrepancy due to the low-Reynolds-number effect. The turbulent fluctuation significantly increases with Re_τ. The mesh resolution is critical to predict the flow quantities correctly.

Acknowledgments

This work has been financially supported by the *Ministerio de Ciencia e Innovación*, Spain (ENE2010-17801). Hao Zhang would like to acknowledge the FI-AGAUR doctorate scholarship granted by the Secretaria d'Universitats i Recerca (SUR) del Departament d'Economia i Coneixement (ECO) de la Generalitat de Catalunya, and by the European Social Fund. F. Xavier Trias would like to thank the financial support by the *Ramón y Cajal* postdoctoral contracts (RYC-2012- 11996) by the *Ministerio de Ciencia e Innovación*. Calculations have been performed on the IBM MareNostrum supercomputer at the

Barcelona Supercomputing Centre. The authors thankfully acknowledge these institutions.

We also thank the anonymous reviewers for their comments and remarks which helped to improve the quality of this work.

References

[1] J. Nikuradse, Untersuchung über die Geschwindigkeitsverteilung in turbulenten Strömungen, Vdi-verlag, 1926.

[2] S. Gavrilakis, Numerical simulation of low-Reynolds-number turbulent flow through a straight square duct, Journal of Fluid Mechanics 244 (1992) 101–129.

[3] Y. Joung, S.-U. Choi, J.-I. Choi, Direct numerical simulation of turbulent flow in a square duct: analysis of secondary flows, Journal of Engineering Mechanics 133 (2) (2007) 213–221.

[4] A. Pinelli, M. Uhlmann, A. Sekimoto, G. Kawahara, Reynolds number dependence of mean flow structure in square duct turbulence, Journal of Fluid Mechanics 644 (2010) 107–122.

[5] H. Xu, Direct numerical simulation of turbulence in a square annular duct, Journal of Fluid Mechanics 621 (2009) 23–57.

[6] R. K. Madabhushi, S. Vanka, Large eddy simulation of turbulence-driven secondary flow in a square duct, Physics of Fluids A: Fluid Dynamics (1989-1993) 3 (11) (1991) 2734–2745.

[7] H. Xu, A. Pollard, Large eddy simulation of turbulent flow in a square annular duct, Physics of Fluids 13 (11) (2001) 3321–3337.

[8] M. Piller, E. Nobile, Direct numerical simulation of turbulent heat transfer in a square duct, International Journal of Numerical Methods for Heat and Fluid Flow 6 (2002) 658–686.

[9] L.-D. Ma, Z.-Y. Li, W.-Q. Tao, Direct numerical simulation of turbulent flow and heat transfer in a square duct with natural convection, Heat and Mass Transfer 44 (2) (2007) 229–250.

[10] J. Pallares, L. Davidson, Large-eddy simulations of turbulent heat transfer in stationary and rotating square ducts, Physics of Fluids 14 (8) (2002) 2804–2816.

[11] M. S. Vázquez, O. Métais, Large-eddy simulation of the turbulent flow through a heated square duct, Journal of Fluid Mechanics 453 (2002) 201–238.

[12] X. Yang, Z.-Y. Li, W.-Q. Tao, Direct numerical simulation of turbulent flow and combined convective heat transfer in a square duct with axial rotation, International Journal of Heat and Mass Transfer 53 (23) (2010) 5400–5410.

[13] J. Pallares, L. Davidson, Large-eddy simulations of turbulent flow in a rotating square duct, Physics of Fluids 12 (11) (2000) 2878–2894.

[14] G. Sharma, D. J. Phares, Turbulent transport of particles in a straight square duct, International Journal of Multiphase Flow 32 (7) (2006) 823 – 837.

[15] H. Zhang, F. X. Trias, Y. Tan, Y.Sheng, A. Oliva, Parallelization of a DEM/CFD code for the numerical simulation of particle-laden turbulent flow, 23rd International Conference on Parallel Computational Fluid Dynamics, Barcelona (2011) 1–5.

[16] H. Zhang, F. X. Trias, A. Gorobets, D. Yang, A. Oliva, Y. Tan, Numerical investigation on particle resuspension in turbulent duct flow via DNS-DEM: Effect of collisions, 11th. World Congress on Computational Mechanics (WCCM XI) (2014) 1–8.

[17] H. Zhang, F. X. Trias, A. Oliva, D. Yang, Y. Tan, Y. Sheng, Effect of collisions on the particle behavior in a turbulent square duct flow, Powder Technology 269 (2015) 320–336.

[18] C. Winkler, S. L. Rani, S. Vanka, Preferential concentration of particles in a fully developed turbulent square duct flow, International Journal of Multiphase Flow 30 (1) (2004) 27 – 50.

[19] C. Winkler, S. L. Rani, Relative importance of the lift force on heavy particles due to turbulence driven secondary flows, Powder Technology 190 (3) (2009) 310 – 318.

[20] A. Huser, S. Biringen, Direct numerical simulation of turbulent flow in a square duct, Journal of Fluid Mechanics 257 (1993) 65–95.

[21] A. Huser, S. Biringen, F. F. Hatay, Direct simulation of turbulent flow in a square duct: Reynolds-stress budgets, Physics of Fluids 6 (9) (1994) 3144–3152.

[22] Z. Zhu, H. Yang, T. Chen, Direct numerical simulation of turbulent flow in a straight square duct at Reynolds Number 600, Journal of Hydrodynamics, Ser. B 21(5) (2009) 600–607.

[23] W. Lo, C.-A. Lin, Mean and turbulence structures of Couette-Poiseuille flows at different mean shear rates in a square duct, Physics of Fluids 18 (6) (2006) 068103.

[24] H.-W. Hsu, F.-N. Hwang, Z.-H. Wei, S.-H. Lai, C.-A. Lin, A parallel multilevel preconditioned iterative pressure Poisson solver for the large-eddy simulation of turbulent flow inside a duct, Computers & Fluids 45 (1) (2011) 138–146.

[25] H.-W. Hsu, J.-B. Hsu, W. Lo, C.-A. Lin, Large eddy simulations of turbulent Couette–Poiseuille and Couette flows inside a square duct, Journal of Fluid Mechanics 702 (2012) 89–101.

[26] M. Kim, D. You, Reynolds number effect on turbulent secondary flow in a duct, Journal of Mechanical Science and Technology 28 (4) (2014) 1311–1318.

[27] H. Raiesi, U. Piomelli, A. Pollard, Evaluation of turbulence models using direct numerical and large-eddy simulation data, Journal of Fluids Engineering 133 (2) (2011) 021203.

[28] Z. Zhu, H. Yang, T. Chen, Numerical study of turbulent heat and fluid flow in a straight square duct at higher Reynolds numbers, International Journal of Heat and Mass Transfer 53 (1) (2010) 356–364.

[29] M. Rokni, T. B. Gatski, Predicting turbulent convective heat transfer in fully developed duct flows, International Journal of Heat and Fluid Flow 22 (4) (2001) 381–392.

[30] M. Fairweather, J. Yao, Large eddy simulation of particle dispersion in a straight, square duet flow, Computer Aided Chemical Engineering 25 (2008) 829–834.

[31] J. Adams, M. Fairweather, J. Yao, Modelling and simulation of particle re-suspension in a turbulent square duct flow, Computers and Chemical Engineering 35 (5) (2011) 893 – 900.

[32] R. W. C. P. Verstappen, A. E. P. Veldman, Symmetry-preserving discretization of turbulent flow, Journal of Computational Physics 187 (2003) 343–368.

[33] F. X. Trias, O. Lehmkuhl, A self-adaptive strategy for the time integration of Navier-Stokes equations, Numerical Heat Transfer, Part B: Fundamentals 60 (2) (2011) 116–134.

[34] A. J. Chorin, Numerical solution of the Navier-Stokes equations, Journal of Computational Physics 22 (1968) 745–762.

[35] A. Gorobets, F. Trias, R. Borrell, O. Lehmkuhl, A. Oliva, Hybrid MPI+OpenMP parallelization of an FFT-based 3D Poisson solver with one periodic direction, Computers & Fluids 49 (1) (2011) 101–109.

[36] F. X. Trias, M. Soria, A. Oliva, C. D. Pérez-Segarra, Direct numerical simulations of two- and three-dimensional turbulent natural convection flows in a differentially heated cavity of aspect ratio 4, Journal of Fluid Mechanics 586 (2007) 259–293.

[37] M. Uhlmann, A. Pinelli, G. Kawahara, A. Sekimoto, Marginally turbulent flow in a square duct, Journal of Fluid Mechanics 588 (2007) 153–162.

[38] P. Moin, K. Mahesh, Direct numerical simulation: A tool in turbulence research, Annual Review of Fluid Mechanics 30 (1998) 539–578.

[39] G. Grötzbach, Revisiting the resolution requirements for turbulence simulations in nuclear heat transfer, Nuclear Engineering and Design 241 (11) (2011) 4379–4390.

[40] A. W. Vreman, J. G. M. Kuerten, Comparison of direct numerical simulation databases of turbulent channel flow at $Re_\tau = 180$, Physics of Fluids 26 (1) (2014) 015102.

[41] M. Quadrio, P. Luchini, Integral space-time scales in turbulent wall flows, Physics of Fluids 15 (8) (2003) 2219–2227.

[42] J. Hartnett, J. Koh, S. McComas, A comparison of predicted and measured friction factors for turbulent flow through rectangular ducts, Journal of Heat Transfer 84 (1) (1962) 82–88.

[43] O. C. Jones, An improvement in the calculation of turbulent friction in rectangular ducts, Journal of Fluids Engineering 98 (2) (1976) 173–180.

[44] J. Kim, P. Moin, R. Moser, Turbulence statistics in fully developed channel flow at low Reynolds number, Journal of Fluid Mechanics 177 (1987) 133–166.

[45] M. M. Rai, P. Moin, Direct simulations of turbulent flow using finite-difference schemes, Journal of Computational Physics 96 (1) (1991) 15–53.

[46] A. Popovich, R. Hummel, Experimental study of the viscous sublayer in turbulent pipe flow, AIChE Journal 13 (5) (1967) 854–860.

[47] P. H. Alfredsson, A. V. Johansson, J. H. Haritonidis, H. Eckelmann, The fluctuating wall-shear stress and the velocity field in the viscous sublayer, Physics of Fluids (1958-1988) 31 (5) (1988) 1026–1033.